A transformative strategy to realize hydrogen production with electricity output through ultra-low potential furfural oxidation on hollow PdCu alloy networks

Xin Zhang [a,1], Tian-Yang Liu [b,1], Ying Zhou [a], Lu Zhang [a,*], Xiao-Cheng Zhou [b,*], Jiu-Ju Feng [a], Ai-Jun Wang [a,*]

[a] *Key Laboratory of the Ministry of Education for Advanced Catalysis Materials, College of Chemistry and Materials Sciences, College of Geography and Environmental Sciences, Zhejiang Normal University, Jinhua 321004, China*
[b] *Jiangsu Collaborative Innovation Centre of Biomedical Functional Materials, Jiangsu Key Laboratory of New Power Batteries, School of Chemistry and Materials Science, Nanjing Normal University, Nanjing 210023, China*

ARTICLE INFO

ABSTRACT

It is of sustainable prominence for building an electrocatalytic system to generate hydrogen (H_2) with low energy consumption. Herein, interconnected hollow PdCu alloy networks (H-PdCu ANs) are fabricated *via* Kirkendall-effect during the cyanogel-reduction procedure. The H-PdCu ANs catalyze furfural oxidation at ultralow potential (0.1 V_{RHE}), and facilitate hydrogen atom releasing from the aldehyde groups, eventually harvesting H_2. Likewise, the typical catalyst exhibits superior oxygen reduction activity with a positive onset potential of 1.0 V_{RHE} and half-wave potential of 0.88 V_{RHE}. Density functional theory calculations are carried out to illustrate the reaction mechanisms. Subtle integration of the two half-reactions, the catalyst-assembled electrocatalytic system concurrently generate H_2 (5 mmol A^{-1} g^{-1} h^{-1}), high value-added furoic acid (93.3% of Faraday efficiency) and electricity (16.2 mW cm^{-2}), overturning conventional H_2 generation system with electricity input. This work provides transformative insights into developing bifunctional electrocatalysts to synchronously realize H_2 generation, biomass upgrading and power output.

1. Introduction

With rapid development of modern society and severe environment pollution, it is increasingly prominent to search green and economic energy with abundant sources [1]. As a high-purity, no pollution and sustainable energy, hydrogen (H_2) energy has attracted worldwide attention because of its rich sources [2,3]. It is highly recognized as a green and sustainable development strategy for producing H_2 by water electrolysis [4]. Nevertheless, the overall efficiency for water electrolysis is seriously inhibited by sluggish anodic oxygen evolution reaction (OER) due to its complicated four-electron transfer process, different from the easier hydrogen evolution reaction (HER) [5]. As alternatives, substantial efforts have been made to reduce energy consumption by using thermodynamically favorable small molecule oxidation reactions instead of anodic OER for H_2 production [6,7].

In recent years, biomass upgrading has received increasing attention

for its lower oxidation potential to achieve a green carbon-neutral economy [8,9]. Apart from the target H_2, high-valued biological by-products can be also harvested during biomass oxidation reaction (BOR) process, coupled with the less power consumption [10,11]. Lately, an electrocatalytic system was built for H_2 production only with an input voltage of 0.98 V, which is much lower than that of theory (1.23 V), coupled by generation of high value-added gluconic acid from glucose oxidation [12].

Conventional electrolysis systems for organic oxidation and H_2 production still require high voltage input ($\sim$ 1 V), albeit with great promise and progress already made for the BOR-involved water electrolysis [13]. Fortunately, such a secure barrier is inspiringly breached by using Cu/Cu foam as anode for furfural oxidation to furoic acid with ultra-low-potential ($\sim$ 0.1 V_{RHE}) under alkaline conditions, which blaze a new trail of BOR [14]. Interestingly, as the C-H bond is broken from the aldehyde group in furfural at a lower potential, the resulting hydrogen

atom (H*) can be recombined together to generate H_2 ($H^* + H^* = H_2$) instead of being oxidized to water ($H^* + OH^- = H_2O + e^-$) [15], ultimately harvesting high-purity H_2 and high-valued by-products with a less energy consumption. Moreover, the cleavage of C-H bond into H_2 is also realized by other metals such as Ag [16], Au [17] and Pd [18] in alkaline solution.

To drive gratifying BOR at a lower potential, development of high-efficiency electrocatalysts is the vital point by finely modulating the electronic structures (e.g., electron density, orbital hybridization state, surface energy, etc.). To achieve improved performance, alloying target material with other dopant is one of the effective strategies [19,20]. However, it is difficult to obtain homogeneous alloyed materials by a common wet-chemistry method, due to great difference in the reduction potentials between the target and dopant. Therefore, thermal treatment is often required with assistance of a complexing agent, which would inevitably cause a waste of energy and sometimes serious agglomeration of the metal nanoparticles. Also, the involved ligand would more or less

cover the catalyst surface to even occupy the active sites, thereby being detrimental to the catalytic property [21].

According to our previous research, different metals are uniformly complexed at an atomic level in the interconnected transition-metal cyanogel with three-dimensional (3D) framework [22], without any additional complexing agent. Upon direct reduction, the precursors are concurrently reduced and in-situ entrapped by the cyanogel skeleton, avoiding their random migration during the reaction process, eventually forming highly homogeneous alloyed structure [23]. Further, the alloying degree can be finely regulated by adopting proper reducing agent and dopant embedded in the cyanogel skeleton [24].

On this basis, we novelly engaged Cu-based PdCu cyanogel as the framework precursor to prepare 3D interconnected hollow PdCu alloy networks (H-PdCu ANs). The bifunctional catalytic activity of the H-PdCu ANs was critically examined by using furfural oxidation and oxygen reduction reaction (ORR) as benchmarked models, combined by scrupulously illustrating the catalytic reaction mechanism through
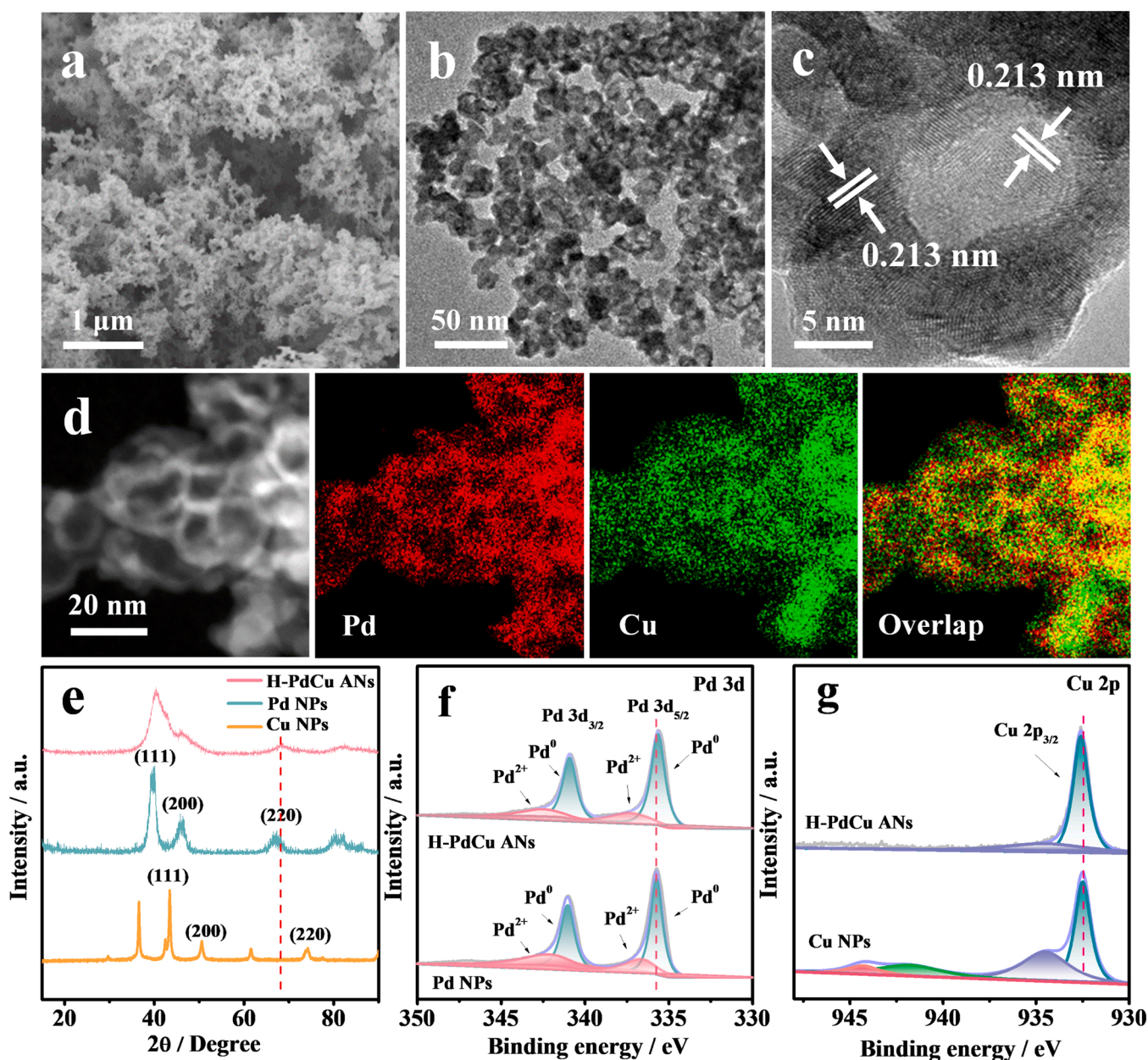
Fig. 1. a) SEM image. b) Low- and c) HR-TEM images of the H-PdCu ANs. d) HAADF-STEM and corresponding EDS mapping images. e) XRD patterns of H-PdCu ANs, Pd NPs, and Cu NPs. f) High-resolution Pd 3d XPS spectra in Pd NPs and H-PdCu ANs. g) The Cu 2p XPS segments in H-PdCu ANs and Cu NPs.

density functional theory (DFT). In the end, the 3D H-PdCu ANs catalyst was employed for assembly of the electrocatalytic system involving the BOR and ORR to evaluate H_2 production, biomass upgrading and concomitant power generation.

2. Experimental section

2.1. Synthesis of 3D H-PdCu ANs

The H-PdCu ANs were prepared by reducing the fresh $K_2Pd(CN)_4$/$CuCl_2$ cyanogel with $NaBH_4$. First, 3.0 mL of a 0.05 M $K_2Pd(CN)_4$ solution and 3.0 mL of a 0.05 M $CuCl_2$ solution were uniformly mixed and ultrasonicated at 30 °C to produce a blue gel-like $K_2Pd(CN)_4$/$CuCl_2$ cyanogel (shown in Fig. 1a), combined by dropwise addition of a freshly-prepared $NaBH_4$ aqueous solution (6 mL, 0.033 mg/mL). The color of the gel turns from blue to black immediately. The solution was kept stirring for 30 min and then remained for 9 h at 30 °C. The derived black powder was repeatedly washed with 0.5 M H_2SO_4, water and ethanol for several times, and then dried overnight in vacuum at 60 °C.

In the controls, Cu NPs and Pd NPs were prepared with single metal precursor in the controlled experiments. For preparation of PdCu NPs, the precursor solution was derived by mixing $PdCl_2$ (0.05 M) and $CuCl_2$ (0.05 M) together. All of the controlled samples were obtained under the other identical conditions if not stated otherwise.

2.2. Preparation of the H-PdCu ANs modified electrodes

For preparing the H-PdCu ANs ink, 5 mg of the catalyst was dispersed in 0.47 mL of water, 0.50 mL of ethanol and 30 μL of a Nafion solution (5 *wt*%) under ultrasonication for 30 min. Then, 20 μL of the catalyst link was dropped onto a cleaned glassy carbon rotating disk electrode (RDE, $\Phi = 5$ mm) with a catalyst loading of 0.50 mg cm^{-2}. In parallel, the Pd NPs, Cu NPs and PdCu NPs modified electrodes were constructed in a similar way for comparison.

For assembly of the electrocatalytic system, the H-PdCu ANs immobilized electrode was typically prepared on carbon cloth (1.0 × 1.0 cm^{-2}) with the prepared catalyst ink and obtained after drying. The average catalyst loading was 1.0 mg cm^{-2}.

More detailed information of *Chemicals, Characterization, Electrochemical measurements, Electrocatalytic system test* and *Computational methods* were presented in the Supporting Information (SI).

3. Results and discussion

3.1. Characterizations

Initially, a blue uniform gel-like mixture was obtained through the reaction between the colorless $K_2Pd(CN)_4$ and light-blue $CuCl_2$ solution (Fig. S1a). The resulting gel was strictly examined by Fourier transform infrared (FT-IR) spectroscopy (Fig. S2), where a strong vibration peak at 2187 cm^{-1} evidently manifests the existence of the Pd-CN-Cu bonds, showing entire 3D skeleton of the cyanogel formed (Fig. S1b) [25,26].

The scanning electron microscopy (SEM) and transmission electron microscopy (TEM) images show the unique 3D interconnected coral-like structures (Fig. 1a), thanks to the direct reduction of the cyanogel along the backbone, as supported by our previous research [22]. In contrast, PdCu NPs, prepared without the cyanogel, show randomly dispersed particle-connected structures (Fig. S3), further proving the necessity of the cyanogel in this preparation.

As further illustrated by the TEM image (Fig. 1b), there emerge many hollow nanoparticles with internal cavities and uniform shells for the H-PdCu ANs. Integration with the evenly distributed Pd and Cu elements in the particle shell (Fig. 1d), the hollow structure is definitely certified by the subsequent high-resolution TEM (HR-TEM, Fig. 1c). Moreover, the corresponding lattice fringes are clearly observed with an interplanar spacing of 0.213 nm, matching well with the (111) facets of the PdCu

alloy [27]. It is worth noting that the spacing of the Pd (111) planes in H-PdCu ANs is smaller than that of bulk Pd (0.225 nm), indicating the successful incorporation of Cu into Pd lattices in H-PdCu ANs [28].

In order to investigate the influence of the Cu doping, X-ray diffraction (XRD) patterns of the H-PdCu ANs, Cu NPs, Pd NPs and PdCu NPs were recorded. As shown in Fig. 1e, the H-PdCu ANs sample exhibits the characteristic diffraction peaks of only Pd at 40.40°, 46.62°, 68.53° and 82.35° corresponding to the (111), (200), (220) and (311) facets of face-centered cubic Pd, respectively, without any independent signal from Cu, which indicates the formation of the PdCu alloy [29]. In contrast, the XRD pattern of PdCu NPs shows the combined peaks of individual Pd and Cu (Fig. S4), conversely confirming the indispensability of cyanogel precursor for *in-situ* forming the homogeneous alloy. Moreover, the peaks of H-PdCu ANs slightly move to the higher degree as compared with those of Pd NPs, due to the smaller atomic radius of Cu itself [30]. Accordingly, the alloying degree of Cu in H-PdCu ANs is calculated to be 21.8 at% (Eq. S3-4, see details in SI) [31], in line with the analysis by energy dispersive spectroscopy (EDS, Fig. S5) with 23.9 at% Cu and 76.1 at% Pd.

After alloying, the surface chemical states of H-PdCu ANs were also examined by X-ray photoelectron spectroscopy (XPS) [32]. As shown in Fig. 1f, the peaks at 335.6 eV (Pd $3d_{5/2}$) and 340.9 eV (Pd $3d_{3/2}$) are attributed to metallic Pd, while those at 337.2 eV (Pd $3d_{5/2}$) and 342.5 eV (Pd $3d_{3/2}$) correspond to ionic Pd [20,27]. As well, the peak at 934.5 eV stems from Cu^{2+} species in the Cu $2p_{3/2}$ section (Fig. 1g) [33, 34]. The peak at ~932.6 eV has the lower binding energy, manifesting the presence of Cu^0 or Cu^+ species in the H-PdCu ANs. As known, it is difficult to distinguish the Cu^0 and Cu^+ states by XPS analysis for their similar binding energies. Therefore, we carefully checked the existence of Cu^0 and Cu^+ or not by Cu LMM X-ray excited auger spectroscopy (XEAS). Fig. S6 shows the peaks at the kinetic energies of 918.4 eV and 916.1 eV, which are well assigned to the Cu^0 and Cu^+ [35], respectively. Namely, Cu^0 is the main predominant valence in H-PdCu ANs, accompanied with smaller amounts of Cu^+ and Cu^{2+} in the sample resulted from the partial oxidation in the air [27]. Notably, as compared to monometallic Pd NPs and Cu NPs, the binding energies of Pd and Cu in the H-PdCu ANs are gradually shifted to more negative and positive directions (Fig. 1f and g), respectively, indicating the effective charges transfer between Pd and Cu for their different electronegativity. As a result, the surface energy is well regulated, finally promoting the electrocatalytic reactions [36,37].

For illuminating the formation mechanism of the H-PdCu ANs, we first supervised the reduction procedures of different precursors with $NaBH_4$ (Fig. 2a). Concisely, the blue cyanogel is immediately reduced to black powder upon addition of the fresh $NaBH_4$ solution, and a similar phenomenon is observed in the case of $CuCl_2$. However, there is almost no change within 30 min for the $K_2Pd(CN)_4$ solution, followed by very slow appearance of a black precipitate as time goes on. These scenarios can be explained by the easier reduction of $CuCl_2$ ($E = 0.70$ V$_{RHE}$, Fig. S7a) than $K_2Pd(CN)_4$ ($E = 0.26$ V$_{RHE}$, Fig. S7b) in the identical environment. For the reduction of PdCu cyanogel, Cu core is foremost formed, accompanied by the reduction of the Pd precursor *via* galvanic replacement to harvest a typical Cu-Pd core/shell structure.

In the meantime, the elemental distributions were mapped at different reaction time to further illustrate the formation mechanism of the H-PdCu ANs (Fig. 2b). Consistently, the core-shell structure is observed for the particles obtained at 3 h, where Cu behaves as the inner core while Pd as the external shell. When the time extends to 6 h, many hollow structures show up, reflecting the gradual diminishment of the core-shell architectures. Finally, there appear high-density PdCu particles with hollow structures when the time proceeds up to 9 h, while there hardly shows any core-shelled particles.

According to the above analysis, the galvanic displacement and Kirkendall effect synergistically account for the formation of the alloyed hollow structure (Fig. 2c) [38,39]. Briefly, the Cu salt is first reduced upon addition of $NaBH_4$ and yields small Cu particles by extending the
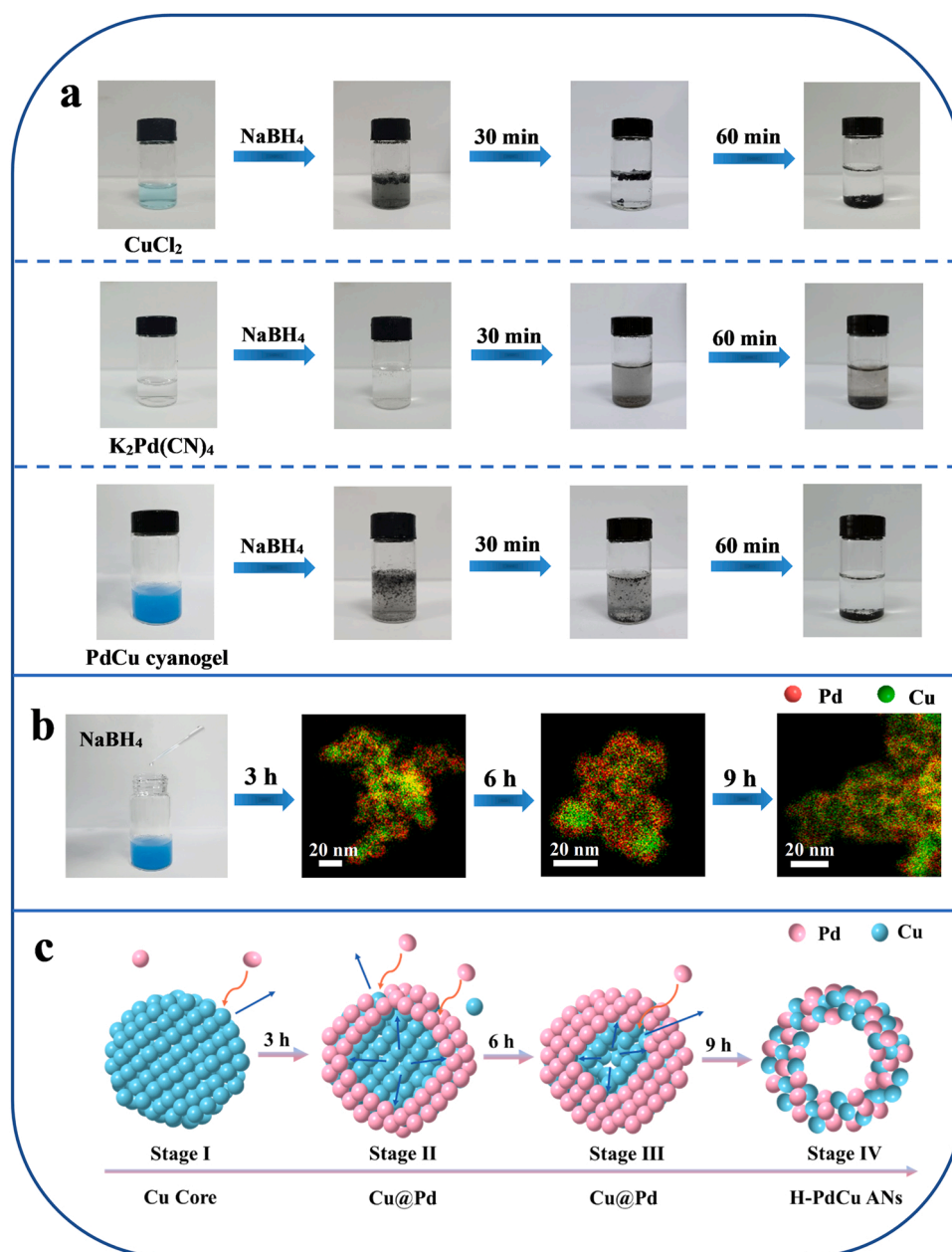
Fig. 2. a) The photographs of the $CuCl_2$ solution, $K_2Pd(CN)_4$ solution and PdCu cyanogel after the addition of $NaBH_4$ for different time periods. b) HAADF-STEM-EDS elemental mappings of the derived samples after reduction of PdCu cyanogel for 3 h, 6 h and 9 h. c) Schematic diagram of the formation mechanism of H-PdCu ANs.

reaction time. Then, the Pd precursor is gradually reduced by the adjacent Cu atom through the displacement reaction for their different reduction potentials, eventually forming the core-shell structure [40]. The unique architecture is mainly resulted from the fact that the smaller radius of Cu would have a greater outward diffusing rate than that of the inward diffused Pd [41]. Therefore, the Kirkendall effect expounds for the outward migration of the inner Cu core to the outer Pd layer until its complete disappearance, finally forming the PdCu alloyed hollow structure.

3.2. Electrochemical BOR measurements

To construct a novel H_2 production system with a high-power output, BOR at an ultralow potential is the key point under alkaline condition, where low-potential oxidation of furfural worked as the benchmarked model. Fig. 3a shows the linear sweep voltammetry (LSV) curves of the investigated catalysts towards furfural oxidation in 0.1 M KOH electrolyte. Plainly, the onset potential (E_{onset}) of the 3D H-PdCu ANs is only about 0.1 V_{RHE}, which is more negative than that of the home-made Pd NPs, coupled by hardly showing any signal in the case of Cu NPs (Fig. 3a). As an anodic competitive reaction, the E_{onset} of OER (> 1.5 V_{RHE}) is much high regardless presence of furfural or not, indicating that furfural oxidation occurs preferentially at a lower potential (Fig. S8a). As expected, H-PdCu ANs catalyst can drive the furfural oxidation reaction at ultralow potentials (Fig. 3b), outperforming that of the Pd NPs catalyst with identical current densities.

The gas product on the H-PdCu ANs was well collected during the low-potential anodizing reaction process, whose gaseous components were analyzed by gas chromatography (GC). As shown in Fig. 3c, a distinct peak emerges at around 0.9 min, which is assigned to the existence of H_2 generated during the reaction. As the absence of furfural hardly yields any signals at the lower potentials (Fig. S8b), the H_2 is apparently derived from the recombination of H* by the C-H cleavage in furfural, rather than the water splitting.
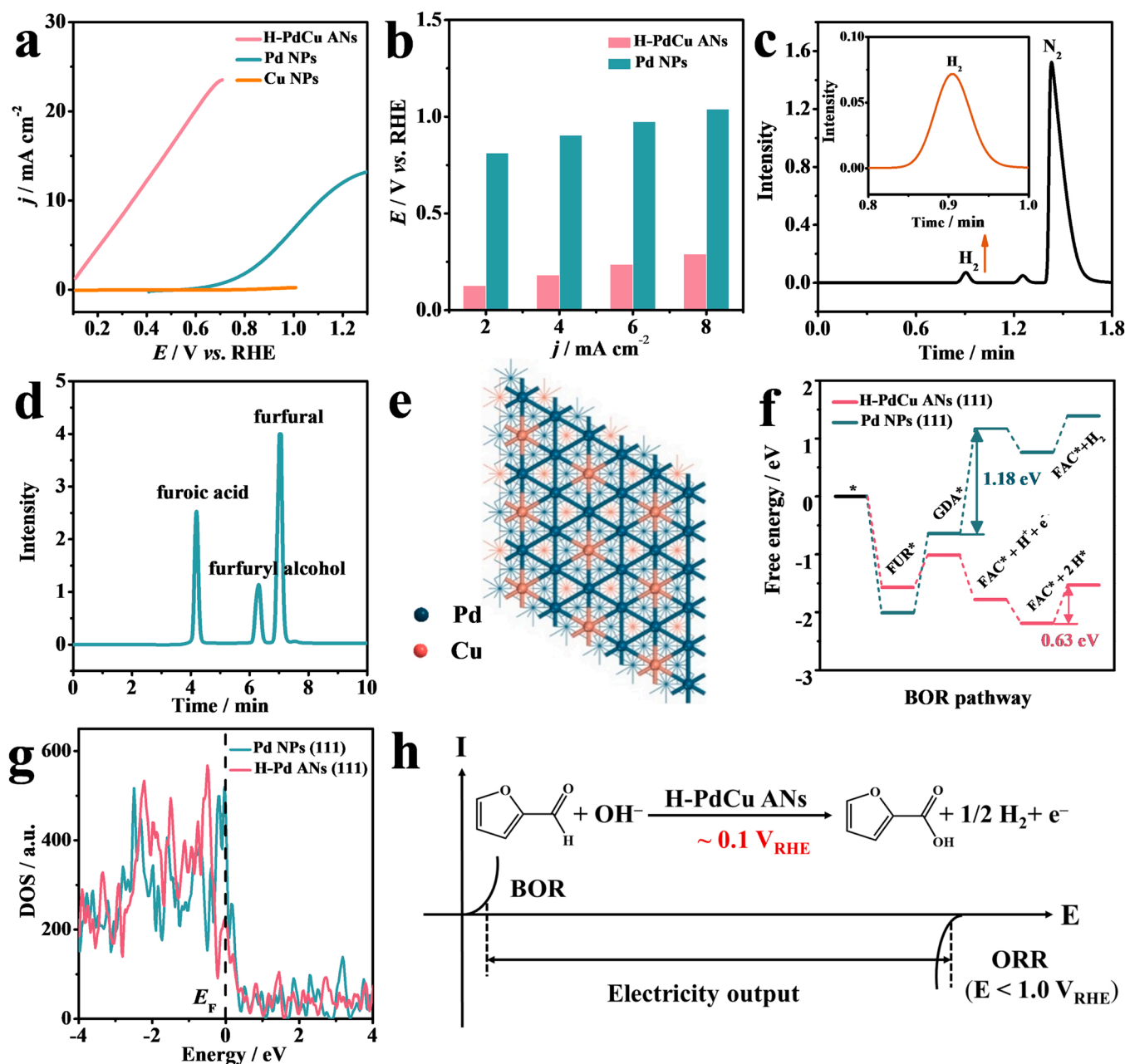
Fig. 3. a) LSV curves of furfural electrooxidation on H-PdCu ANs, Pd NPs and Cu NPs modified electrodes. b) Potentials required for the furfural oxidation at different current densities on H-PdCu ANs and Pd NPs. c) Gas chromatogram of the gas products generated from the furfural oxidation on H-PdCu ANs. d) HPLC curve of the anolyte. e) The adsorption model about the H-PdCu ANs (111) surface. f) Corresponding free energy diagrams of low-potential furfural oxidation on the Pd (111) surface of H-PdCu ANs and Pd NPs. g) The DOS for 3d orbitals of active Pd atom on Pd (111) surface of H-PdCu ANs and Pd NPs. h) The developed electricity output mode.

Furthermore, Fig. 3d depicts the compositions of the liquid product investigated by high-performance liquid chromatography (HPLC), including furoic acid derived from furfural oxidation and a small amount of furfuryl alcohol produced by the Cannizzaro disproportionation of furfural (2R-CHO + H$_2$O = R-COOH + R-CH$_2$OH) at the early reaction stage under the alkaline conditions [42].

Notably, the hydrogen atoms cleaved from furfural are more likely to form H$_2$ by the low-potential oxidation on H-PdCu ANs, rather than oxidizing to H$_2$O. To gain more insights into the reaction mechanism from a fundamental viewpoint, the density functional theory (DFT) calculations were performed on the Pd (111) surface of H-PdCu ANs (Fig. 3e) and Pd NPs (Fig. S9).

Presumably, the furfural oxidation at the lower potential undergoes

several reaction pathways, including geminal diols in the alkaline media [14] (Eq. S5-9, see details in SI). First, the geminal diols are formed *via* a hydration reaction between water and furfural. In the as-formed geminal diols, one of the hydroxy groups is subsequently deprotonated to gem-diolate anions (GDAs) by attracting a hydroxy ion. These unstable GDAs are preferentially adsorb on the Pd (111) surface, followed by breaking the C-H bond to form furoic acid (FAC*) and an adsorbed hydrogen atom (H*). Finally, the highly active H* is preferentially bond each other to form H$_2$ through the Tafel recombination (H* + H* → H$_2$) at a lower potential, associated with the released furoic acid from the catalyst surface [15].

Accordingly, we critically studied the behaviors of the furfural oxidation on the H-PdCu ANs and Pd NPs by the DFT analysis. Fig. 3f

shows their different rate-determining step (RDS). For H-PdCu ANs, an energy barrier of 0.63 eV is required in the last step for generating H_2, which is identified as the RDS. As compared, the splitting of GDAs to FAC* and H* is the RDS for Pd NPs, which demands a much larger energy barrier of 1.81 eV. Clearly, H-PdCu ANs catalyst is more inclined to generate furoic acid and H_2, which is attributed to the electron redistribution of Pd by doping Cu.

By virtue of the strong coupling between Cu and Pd, the center of the *d*-band in H-PdCu ANs shows obviously negative shifts (Fig. 3g and Fig. S10), indicating the accelerated electron transfer, which is consistent with the XPS analysis [43]. With the superior activity of H-PdCu ANs towards furfural oxidation, it shows a possibility to build an electrocatalytic system by employing H-PdCu ANs as efficient bifunctional catalyst, concurrently realizing the electricity output and H_2 production (Fig. 3h). Now, the point comes to the ORR ability given by H-PdCu ANs.

3.3. Electrochemical ORR measurements

To be a promising candidate, the ORR activity of H-PdCu ANs was first evaluated by linear sweep voltammetry (LSV) in the O_2-saturated 0.1 M KOH solution (Fig. 4a). Concisely, the H-PdCu ANs catalyst exhibits a superior ORR activity with the E_{onset} of 1.0 V_{RHE} and half-wave potential ($E_{1/2}$) of 0.88 V_{RHE} over those of the Pd NPs (E_{onset} = 0.98 V_{RHE}; $E_{1/2}$ = 0.87 V_{RHE}) and Cu NPs (E_{onset} = 0.68 V_{RHE}; $E_{1/2}$ = 0.51 V_{RHE}), thanks to the well-adjusted electronic structure of Pd with the incorporated Cu. In addition, the limiting current density (j_L = 6.0 mA cm^{-2}) is the highest for H-PdCu ANs among the catalysts, mainly attributing to the unique 3D interconnected hollow structure with abundant active sites [44]. As further illustrated in Fig. S11, the PdCu

NPs catalyst has a much inferior ORR activity to the target H-PdCu ANs, which indicates that the cyanogel precursor is of great importance for *in-situ* producing the favorite alloyed structure.

Apart from the excellent E_{onset} and $E_{1/2}$, the Tafel slope of H-PdCu ANs (62.9 mV dec^{-1}) is also the lowest among the catalysts (Fig. 4b), indicating the highly accelerated kinetics during the ORR process. Consistently, the following electrochemical impedance spectroscopy (EIS) plots (Fig. 4c) depict that the H-PdCu ANs has the smallest charge transfer resistance (R_{ct}), showing the fastest ORR kinetics, due to the high alloy and 3D interconnected structure [45,46].

To evaluate the possibility of the electrocatalyst for practical applications, long-term stability of H-PdCu ANs was also assessed for the ORR (Fig. 4d). After repeated scanning for 2000 cycles, the $E_{1/2}$ shows a negligible negative shift of only 11 mV, almost maintaining the initial performance. As well, the j_L remains 96.5% of its original value after the chronoamperometry test for 10 h (inset in Fig. 4d), further confirming the outstanding durability towards the ORR. The remarkable stability is primarily ascribed to the extraordinary solid 3D interconnected structure, which effectively prevents the particle aggregation or even collapse of the unique structure during the ORR process. In parallel, the 3D structure can create abundant channels for timely removal of the generated substances, ensuring a "clean" surface for the follow-up reaction.

Theoretically, the ORR follows direct 4-electron transfer or indirect 2-electron transfer pathway (Eq. S10-15, as described in SI). Particularly, the 4-electron transfer pathway has a higher efficiency in constructing the ORR-related devices [47]. Therefore, the ORR activity was rigorously predicted by the DFT calculation with the above-mentioned model.
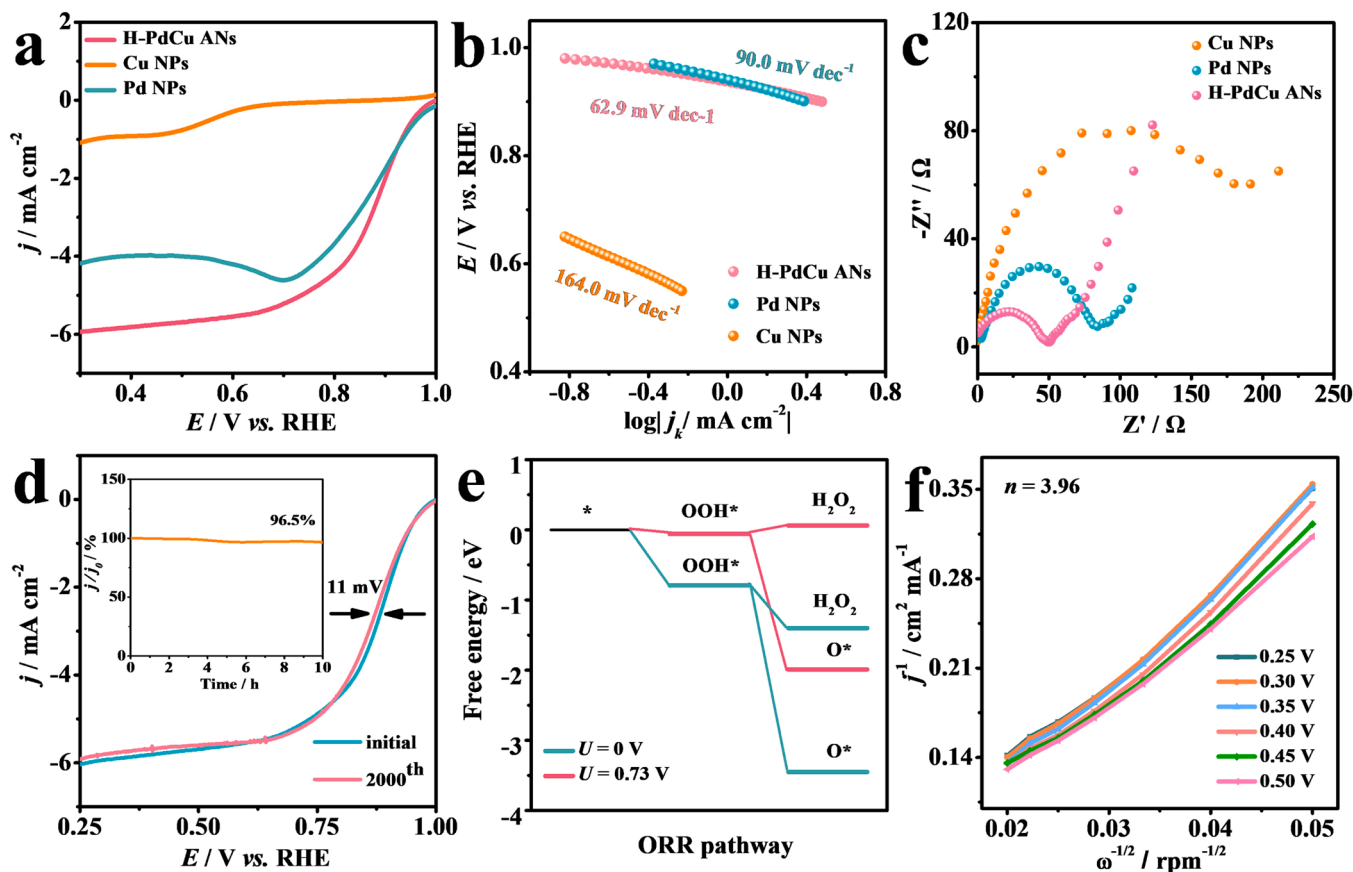

Fig. 4. a) LSV curves of the catalysts recorded in the O_2-saturated 0.1 M KOH solution at 1600 rpm and 10 mV s^{-1}. b) The corresponding Tafel plots. c) Nyquist plots at 0.7 V_{RHE}. d) LSV curves of H-PdCu ANs before and after 2000 cycles. Inset: Chronoamperometric responses of the H-PdCu ANs measured at 0.6 V_{RHE}. e) Gibbs free energy diagram of the ORR process on H-PdCu ANs, and the selectivity comparison between two-electron and four-electron reaction pathways. f) The K-L plots at different potentials.

Specifically, the limiting potential (U_L) is calculated to be 0.73 V for H-PdCu ANs (Fig. S12), which is close to that of the Pt (111) surface (0.79 V), revealing a potentially high ORR activity [48,49]. Moreover, it is much easier to proceed the reaction of OOH* →O* through 4-electron transfer on the Pd (111) surface, rather than the formation of H_2O_2 *via* 2-electron transfer pathway (Fig. 4e). When the applied potential comes to 0.73 V, the generation of H_2O_2 can be effectively suppressed to promote the 4-electron transfer reaction, in turn achieving the maximum efficiency. These observations demonstrate the high activity and selectivity for the 4-electron ORR process, as further evidenced by the experimental LSV curves at different rotation rates (Fig. S13). Accordingly, an average electron transfer number (*n*) is about 3.96 from the Koutecky-Levich (K-L) plots (Eq. S1-2, Fig. 4f), agreeing with the DFT prediction.

With the outstanding BOR and ORR activities, H-PdCu ANs catalyst is proved as effective bifunctional electrocatalyst for assembly of a novel electrocatalytic system.

3.4. Assembly of the BOR/ORR electrocatalytic system

Integration of the low-potential furfural oxidation with the ORR enables a novel electricity output system, synchronously producing H_2 and biomass upgrading, which is different from conventional H_2 generation system with indispensable electricity input. Herein, a homemade H-type cell was assembled by using 3D H-PdCu ANs as the bifunctional BOR/ORR catalysts, in which furfural oxidation occurs on the anode while the ORR is present on the cathode in alkaline environment (Fig. 5a). Ideally, H_2 and furoic acid are produced at the anode, while oxygen is reduced to OH^- at the cathode with electricity output.

Remarkably, the output voltage measured by the multimeter is about 0.88 V for the freshly assembled two-electrode system, in line with the open-circuit voltage (OCV, 0.92 V) detected from the discharge polarization curves, confirming the successful construction of the electrocatalytic system (Fig. 5b and c). Although the output voltage is high, the maximum power density is only 16.2 mW cm^{-2} at a current density of 25.0 mA cm^{-2}, which is smaller than those of the earlier galvanic cells [14,50]. As speculated, the mass transfer and/or proton membrane itself in the H-type cell accounts for the inevitably increased resistance, which would be severely detrimental to the output current density [51,52]. Therefore, more emphasis should focus on developing high-efficiency electrocatalytic system in future industrialization studies.

To assess the stability, the OCV of the assembled system was recorded over time. As seen in Fig. 5d, the OCV remains almost constant for the initial 5 h, and then starts to decay with an initial voltage drop of about 0.3 V within 10 h. As the anodic reactant furfural is gradually consumed, its lower concentration would seriously affect the output voltage of the assembled BOR/ORR cell and even sharply deteriorate the stability. The current H-type cell used here hardly realize the timely and accurate replenishment of furfural, which leads to the decrease of the OCV in the late stage during the long-term operation. Even so, the H-PdCu ANs catalyst undoubtedly exhibits the superior stability during the catalytic procedure, as further evidenced by the almost unchanged morphology after the 10 h-testing (inset in Fig. 5d).

Moreover, the cell stability was also evaluated by the rate capability at different discharge densities (Fig. 5e). When the current densities are modulated, the discharge voltages also change and keep steady at the fixed current densities. Notably, the discharge voltages can return to its initial value upon re-applying the corresponding current densities, demonstrating the remarkable reversibility.

HPLC and GC were employed to analyze the liquid and gaseous products during the operation process. Fig. 5f depicts the concentrations of the organic compounds in the anolyte as a function of the operation
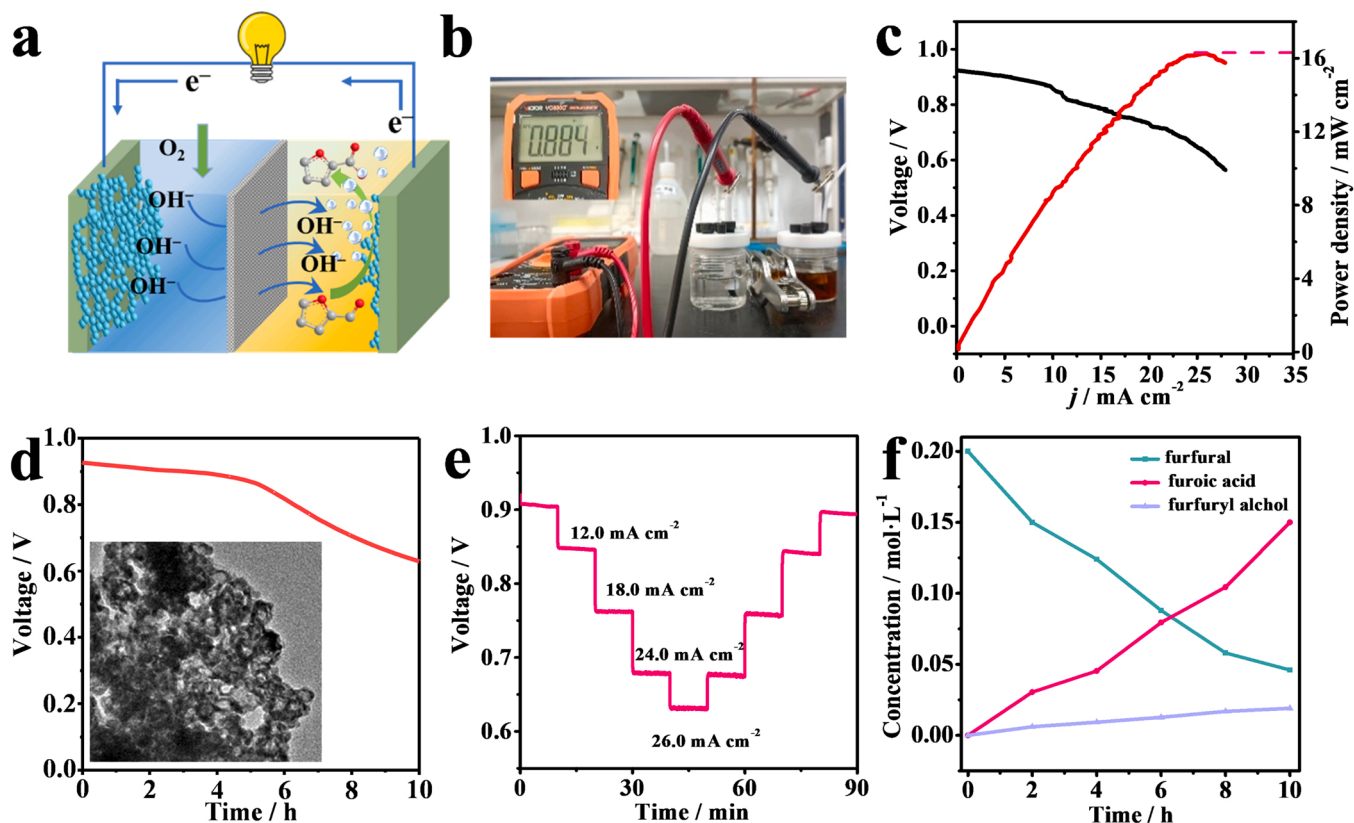
Fig. 5. a) Illustration of the assembled electrocatalytic system by using low-potential furfural oxidation as the anodic reaction and ORR as the cathodic reaction. b) Schematic diagram of the assembled cell based on H-PdCu ANs as bi-functional electrocatalyst. c) Discharge polarization curves and power density curves. d) Image of the open circuit voltage as a function of time for the freshly assembled cell. Inset: the HR-TEM image of the H-PdCu ANs after the operation for 10 h. e) Discharge voltages change with the current densities and time. f) Concentrations of organic compounds in the anolyte as a function of time during the cell operation process.

time. Notably, the content of derived furoic acid is increased with the consumption of furfural, associated with slightly disproportionated furfuryl alcohol in the alkaline condition, which is in accordance with the above-mentioned half-reaction of furfural oxidation. The corresponding Faradaic efficiency (FE) for furoic acid production is calculated to be 93.3% according to Eq. S16 described in SI. In parallel, the yield of H_2 is collected to be 5 mmol A^{-1} g^{-1} h^{-1} for the gaseous product, indicating that the anodic reaction is indeed proceeding as expected upon assembly. Nevertheless, the hydrogen production is relatively far from satisfied, mainly on account of the rudimentary cell limitation especially the overlarge distance between the electrodes and the poor air tightness, as well as the excessive resistance through the proton membrane. Therefore, there is still a long way to go for developing feasible industrial devices albeit with the high-efficiency electrocatalysts.

4. Conclusions

In summary, we developed a novel conversion technology with H-PdCu ANs as a high-efficiency bifunctional catalyst to produce H_2 from electricity input to output. Specifically, the cyanogel precursor and Kirkendall effect played the important roles for forming the interconnected hollow structure, which had abundant channels, apposite electronic structure and ultra-stable framework. As proved by the experimental and theoretical results, the H-PdCu ANs definitely accelerated furfural oxidation at ultralow potential (0.1 V_{RHE}), producing H_2 by recombining H* (liberated from the aldehyde group). Besides, the H-PdCu ANs also possess superior ORR activity, stability, and 4-electron reaction pathway. Subtle combination of the furfural oxidation with the ORR, the H-PdCu ANs assembled system achieved the large H_2 production (5 mmol A^{-1} g^{-1} h^{-1}) and electricity output (16.2 mW cm^{-2}), accompanied by producing high value-added furoic acid (93.3% of FE), overturning conventional H_2 generation driven by electricity input. This study provides a promising strategy to develop bifunctional electrocatalysts for concurrent H_2 generation, biomass upgrading and power output, in turn facilitating the low-carbon economy.

CRediT authorship contribution statement

Xin Zhang: Conceptualization, Methodology, Writing – original draft. **Tian-Yang Liu:** Software, Formal analysis, Data curation. **Ying Zhou:** Formal analysis, Data curation. **Lu Zhang:** Writing – review & editing, Funding acquisition. **Xiao-Cheng Zhou:** Supervision, Funding acquisition. **Jiu-Ju Feng:** Resources. **Ai-Jun Wang:** Project administration.

Declaration of Competing Interest

The authors declare that they have no known competing financial interests or personal relationships that could have appeared to influence the work reported in this paper.

Data Availability

Data will be made available on request.

Acknowledgements

Appendix A. Supporting information

Supplementary data associated with this article can be found in the online version at doi:10.1016/j.apcatb.2023.122530.

References

[1] S. Wu, N. Salmon, M.M.-J. Li, R. Bañares-Alcántara, S.C.E. Tsang, Energy decarbonization via green H_2 or NH_3? ACS Energy Lett. 7 (2022) 1021–1033.

[2] A. Midilli, M. Ay, I. Dincer, M.A. Rosen, On hydrogen and hydrogen energy strategies: I: current status and needs, Renew. Sust. Energ. Rev. 9 (2005) 255–271.

[3] Y. Zhou, R. Li, Z. Lv, J. Liu, H. Zhou, C. Xu, Green hydrogen: a promising way to the carbon-free society, Chin. J. Chem. Eng. 43 (2022) 2–13.

[4] L. Jia, G. Du, D. Han, Y. Hao, W. Zhao, Y. Fan, Q. Su, S. Ding, B. Xu, Ni_3S_2/Cu–NiCo LDH heterostructure nanosheet arrays on Ni foam for electrocatalytic overall water splitting, J. Mater. Chem. A 9 (2021) 27639–27650.

[5] B. Wurster, D. Grumelli, D. Hötger, R. Gutzler, K. Kern, Driving the Oxygen evolution reaction by nonlinear cooperativity in bimetallic coordination catalysts, J. Am. Chem. Soc. 138 (2016) 3623–3626.

[6] C. Tang, R. Zhang, W. Lu, Z. Wang, D. Liu, S. Hao, G. Du, A.M. Asiri, X. Sun, Energy-saving electrolytic hydrogen generation: Ni_2P nanoarray as a high-performance non-noble-metal electrocatalyst, Angew. Chem. Int. Ed. 56 (2017) 842–846.

[7] L. Zhang, D. Lu, Y. Chen, Y. Tang, T. Lu, Facile synthesis of Pd–Co–P ternary alloy network nanostructures and their enhanced electrocatalytic activity towards hydrazine oxidation, J. Mater. Chem. A 2 (2014) 1252–1256.

[8] M. Rehfeldt, E. Worrell, W. Eichhammer, T. Fleiter, A review of the emission reduction potential of fuel switch towards biomass and electricity in European basic materials industry until 2030, Renew. Sust. Energ. Rev. 120 (2020), 109672.

[9] J. Wang, H. Zhao, P. Liu, N. Yasri, N. Zhong, M.G. Kibria, J. Hu, Selective superoxide radical generation for glucose photoreforming into arabinose, J. Energy Chem. 74 (2022) 324–331.

[10] K. Wei, X. Wang, X. Jiao, C. Li, D. Chen, Self-supported 2D Fe-doped Ni-MOF nanosheets as highly efficient and stable electrocatalysts for benzylamine oxidation, Appl. Surf. Sci. 578 (2022), 152065.

[11] Y. Li, X. Wei, L. Chen, J. Shi, Electrocatalytic hydrogen production trilogy, Angew. Chem. Int. Ed. 60 (2021) 19550–19571.

[12] Y. Zhang, B. Zhou, Z. Wei, W. Zhou, D. Wang, J. Tian, T. Wang, S. Zhao, J. Liu, L. Tao, Coupling glucose-assisted Cu (I)/Cu (II) redox with electrochemical hydrogen production, Adv. Mater. 33 (2021) 2104791.

[13] W.J. Liu, Z. Xu, D. Zhao, X.Q. Pan, H.C. Li, X. Hu, Z.Y. Fan, W.K. Wang, G.H. Zhao, S. Jin, Efficient electrochemical production of glucaric acid and H_2 via glucose electrolysis, Nat. Commun. 11 (2020) 1–11.

[14] T. Wang, Z. Huang, T. Liu, L. Tao, J. Tian, K. Gu, X. Wei, P. Zhou, L. Gan, S. Du, Transforming electrocatalytic biomass upgrading and hydrogen production from electricity input to electricity output, Angew. Chem. Int. Ed. 61 (2022), e202115636.

[15] T. Wang, L. Tao, X. Zhu, C. Chen, W. Chen, S. Du, Y. Zhou, B. Zhou, D. Wang, C. Xie, P. Long, W. Li, Y. Wang, R. Chen, Y. Zou, X.Z. Fu, Y. Li, X. Duan, S. Wang, Combined anodic and cathodic hydrogen production from aldehyde oxidation and hydrogen evolution reaction, Nat. Catal. 5 (2022) 66–73.

[16] S. Gao, T. Feng, Q. Wu, C. Feng, N. Shang, C. Wang, Immobilizing AgPd alloy on Vulcan XC-72 carbon: a novel catalyst for highly efficient hydrogen generation from formaldehyde aqueous solution, RSC Adv. 6 (2016) 105638–105643.

[17] X. Pan, L. Wang, F. Ling, Y. Li, D. Han, Q. Pang, L. Jia, A novel biomass assisted synthesis of Au–$SrTiO_3$ as a catalyst for direct hydrogen generation from formaldehyde aqueous solution at low temperature, Int. J. Hydrog. Energy 40 (2015) 1752–1759.

[18] H. Hu, Z. Jiao, J. Ye, G. Lu, Y. Bi, Highly efficient hydrogen production from alkaline aldehyde solutions facilitated by palladium nanotubes, Nano Energy 8 (2014) 103–109.

[19] X. Li, Y. Liu, J.J. Zhang, B. Yan, C. Jin, J. Dou, M. Li, X. Feng, G. Liu, No annealing synthesis of ordered intermetallic PdCu nanocatalysts for boosting formic acid oxidation, Chem. Mater. 34 (2022) 1385–1391.

[20] N. Yang, Z. Zhang, B. Chen, Y. Huang, J. Chen, Z. Lai, Y. Chen, M. Sindoro, A.-L. Wang, H. Cheng, Z. Fan, X. Liu, B. Li, Y. Zong, L. Gu, H. Zhang, Synthesis of ultrathin PdCu alloy nanosheets used as a highly efficient electrocatalyst for formic acid oxidation, Adv. Mater. 29 (2017) 1700769.

[21] S. Li, L. Liu, Q. Zhao, C. He, W. Liu, N-doped graphene-supported PdCu nanoalloy as efficient catalyst for reducing Cr (VI) by formic acid, Phys. Chem. Chem. Phys. 20 (2018) 3457–3464.

[22] M.X. Jin, Y.L. Pu, Z.J. Wang, Z. Zhang, L. Zhang, A.J. Wang, J.J. Feng, Facile synthesis of 3D $NiCoP@NiCoPO_x$ core–shell nanostructures with boosted catalytic activity toward oxygen evolution reaction, ACS Appl. Energy Mater. 2 (2019) 4188–4194.

[23] S.Y. Lin, Y.Q. Yao, L. Zhang, J.J. Feng, A.J. Wang, Cyanogel and its derived-materials: properties, preparation methods, and electrochemical applications, Mater, Today Energy 20 (2021), 100701.

[24] Z.J. Wang, M.X. Jin, L. Zhang, A.J. Wang, J.J. Feng, Amorphous 3D pomegranate-like NiCoFe nanoassemblies derived by bi-component cyanogel reduction for outstanding oxygen evolution reaction, J. Energy Chem. 53 (2021) 260–267.

[25] W. Zhang, X. Zhu, X. Chen, Y. Zhou, Y. Tang, L. Ding, P. Wu, Cyano-bridged coordination polymer hydrogel-derived Sn–Fe binary oxide nanohybrids with

structural diversity: from 3D, 2D, to 2D/1D and enhanced lithium-storage performance, Nanoscale 8 (2016) 9828–9836.

[26] K. Ashley, S. Pons, Infrared spectroelectrochemistry, Chem. Rev. 88 (1988) 673–695.

[27] C. Hu, X. Zhai, Y. Zhao, K. Bian, J. Zhang, L. Qu, H. Zhang, H. Luo, Small-sized PdCu nanocapsules on 3D graphene for high-performance ethanol oxidation, Nanoscale 6 (2014) 2768–2775.

[28] S.F. Ho, A. Mendoza-Garcia, S. Guo, K. He, D. Su, S. Liu, Ö. Metin, S. Sun, A facile route to monodisperse MPd (M = Co or Cu) alloy nanoparticles and their catalysis for electrooxidation of formic acid, Nanoscale 6 (2014) 6970–6973.

[29] L. Zhu, K. Song, C. Yi, One-pot aqueous synthesis of porous hollow PdCu alloy nanoparticles for enhanced ethanol electrooxidation, Inorg. Chem. 61 (2022) 5474–5478.

[30] R. Zhou, X. Fan, X. Ke, J. Xu, X. Zhao, L. Jia, B. Pan, N. Han, L. Li, X. Liu, Two-dimensional palladium–copper alloy nanodendrites for highly stable and selective electrochemical formate production, Nano Lett. 21 (2021) 4092–4098.

[31] G. Zhang, Y. Wang, X. Wang, Y. Chen, Y. Zhou, Y. Tang, L. Lu, J. Bao, T. Lu, Preparation of Pd–Au/C catalysts with different alloying degree and their electrocatalytic performance for formic acid oxidation, Appl. Catal. B-Environ. 102 (2011) 614–619.

[32] W. Zhang, Y.P. Chen, L. Zhang, J.J. Feng, X.S. Li, A.J. Wang, Theophylline-regulated pyrolysis synthesis of nitrogen-doped carbon nanotubes with iron-cobalt nanoparticles for greatly boosting oxygen reduction reaction, J. Colloid Interface Sci. 626 (2022) 653–661.

[33] I.A. Khan, L. Khan, S.I. Khan, A. Badshah, Shape-control synthesis of PdCu nanoparticles with excellent catalytic activities for direct alcohol fuel cells application, Electrochim. Acta 349 (2020), 136381.

[34] H. Shang, H. Xu, Q. Liu, Y. Du, PdCu alloy nanosheets-constructed 3D flowers: new highly sensitive materials for H_2S detection, Sens. Actuators B Chem. 289 (2019) 260–268.

[35] X. Yuan, S. Chen, D. Cheng, L. Li, W. Zhu, D. Zhong, Z.J. Zhao, J. Li, T. Wang, J. Gong, Controllable Cu^0-Cu^+ sites for electrocatalytic reduction of carbon dioxide, Angew. Chem. Int. Ed. 60 (2021) 15344–15347.

[36] L. An, M. Zhu, B. Dai, F. Yu, Hollow palladium-copper bimetallic nanospheres with high oxygen reduction activity, Electrochim. Acta 176 (2015) 222–229.

[37] R. Chen, M. Sun, G. Pang, J. Zhou, L. Hou, F. Gao, Highly active PdCu alloy nanowire network electrocatalyst for ethanol and methanol electrooxidation, ChemElectroChem 4 (2017) 1081–1087.

[38] M.H. Oh, T. Yu, S.H. Yu, B. Lim, K.T. Ko, M.G. Willinger, D.H. Seo, B.H. Kim, M. G. Cho, J.H. Park, K. Kang, Y.E. Sung, N. Pinna, T. Hyeon, Galvanic replacement reactions in metal oxide nanocrystals, Science 340 (2013) 964–968.

[39] Y. Bian, W. Ding, L. Hu, X. Zhu, Y. Sun, Z. Sheng, Magneto-revealing and acceleration of hidden kirkendall effect in galvanic replacement reaction, J. Phys. Chem. Lett. 12 (2021) 5294–5300.

[40] Q. Liu, Z. Li, X. Zhou, J. Xiao, Z. Han, X. Jiang, G. Fu, Y. Tang, Cyanogel-induced PdCu alloy with Pd-enriched surface for formic acid oxidation and oxygen reduction, Adv. Energy Sus. Res. 3 (2022) 2200067.

[41] J.B. Huang, Y.C. Yan, X. Li, X.R. Qiao, X.Q. Wu, J.J. Li, R. Shen, D.R. Yang, H. Zhang, Unexpected kirkendall effect in twinned icosahedral nanocrystals driven by strain gradient, Nano Res. 13 (2020) 2641–2649.

[42] C.D. Hurd, J. Garrett, E. Osborne, Furan reactions. IV. Furoic acid from furfural, J. Am. Chem. Soc. 55 (1933) 1082–1084.

[43] Q. Zhao, L. Liu, R. Liu, L. Zhu, PdCu nanoalloy immobilized in ZIF-derived N-doped carbon/graphene nanosheets: alloying effect on catalysis, Chem. Eng. J. 353 (2018) 311–318.

[44] Y. Liu, H. Li, S. Gong, Y. Chen, R. Xie, Q. Wu, J. Tao, F. Meng, P. Zhao, A novel non-enzymatic electrochemical biosensor based on the nanohybrid of bimetallic PdCu nanoparticles/carbon black for highly sensitive detection of H_2O_2 released from living cells, Sens. Actuators B Chem. 290 (2019) 249–257.

[45] D.C. Martínez-Casillas, G. Vázquez-Huerta, J.F. Pérez-Robles, O. Solorza-Feria, Electrocatalytic reduction of dioxygen on PdCu for polymer electrolyte membrane fuel cells, J. Power Sources 196 (2011) 4468–4474.

[46] N. Ye, Y. Bai, Z. Jiang, T. Fang, Design the PdCu/TaNC electrocatalyst with core-shell structure having high efficiency for methanol and formic acid oxidation reactions, Electrochim. Acta 383 (2021), 138365.

[47] I.S. Amiinu, X. Liu, Z. Pu, W. Li, Q. Li, J. Zhang, H. Tang, H. Zhang, S. Mu, From 3D ZIF nanocrystals to Co–N_x/C nanorod array electrocatalysts for ORR, OER, and Zn–air batteries, Adv. Funct. Mater. 28 (2018) 1704638.

[48] V. Viswanathan, H.A. Hansen, J. Rossmeisl, J.K. Nørskov, Unifying the 2e$^-$ and 4e$^-$ reduction of oxygen on metal surfaces, J. Phys. Chem. Lett. 3 (2012) 2948–2951.

[49] G.S. Karlberg, J. Rossmeisl, J.K. Nørskov, Estimations of electric field effects on the oxygen reduction reaction based on the density functional theory, Phys. Chem. Chem. Phys. 9 (2007) 5158–5161.

[50] Q. Zhou, Z. Shen, C. Zhu, J. Li, Z. Ding, P. Wang, F. Pan, Z. Zhang, H. Ma, S. Wang, Nitrogen-doped CoP electrocatalysts for coupled hydrogen evolution and sulfur generation with low energy consumption, Adv. Mater. 30 (2018) 1800140.

[51] J. Kirner, Y. Chen, H. Liu, J. Song, J. Liao, W. Li, F. Zhao, Exploring electrochemical flow-cell designs and parameters for CO_2 reduction to formate under industrially relevant conditions, J. Electrochem. Soc. 169 (2022), 054511.

[52] S. Liang, N. Altaf, L. Huang, Y. Gao, Q. Wang, Electrolytic cell design for electrochemical CO_2, Reduct., J. CO_2 Util. 35 (2020) 90–105.